RSC Advances

PAPER

View Article Online
View Journal | View Issue

Cite this: *RSC Adv.*, 2023, **13**, 20512

Microfluidic fabrication of X-ray-visible sodium hyaluronate microspheres for embolization†

Yang Shen,[ab] Baoqu Zhang,[ab] Zihan Yi,[ab] Lan Zhang,[ab] Jing Ling,[ab] Shibo Wang,[ab] Zhichao Sun,*[c] M. Zubair Iqbal [ab] and Xiangdong Kong *[ab]

Catheter embolization is a minimally invasive technique that relies on embolic agents and is now widely used to treat various high-prevalence medical diseases. Embolic agents usually need to be combined with exogenous contrasts to visualize the embolotherapy process. However, the exogenous contrasts are quite simply washed away by blood flow, making it impossible to monitor the embolized location. To solve this problem, a series of sodium hyaluronate (SH) loaded with bismuth sulfide (Bi_2S_3) nanorods (NRs) microspheres (Bi_2S_3@SH) were prepared in this study by using 1,4-butaneglycol diglycidyl ether (BDDE) as a crosslinker through single-step microfluidics. Bi_2S_3@SH-1 microspheres showed the best performance among other prepared microspheres. The fabricated microspheres had uniform size and good dispersibility. Furthermore, the introduction of Bi_2S_3 NRs synthesized by a hydrothermal method as Computed Tomography (CT) contrast agents improved the mechanical properties of Bi_2S_3@SH-1 microspheres and endowed the microspheres with excellent X-ray impermeability. The blood compatibility and cytotoxicity test showed that the Bi_2S_3@SH-1 microspheres had good biocompatibility. In particular, the *in vitro* simulated embolization experiment results indicate that the Bi_2S_3@SH-1 microspheres had excellent embolization effect, especially for the small-sized blood vessels of 500–300 and 300 μm. The results showed the prepared Bi_2S_3@SH-1 microspheres have good biocompatibility and mechanical properties, as well as certain X-ray visibility and excellent embolization effects. We believe that the design and combination of this material has good guiding significance in the field of embolotherapy.

Received 28th April 2023
Accepted 27th June 2023

DOI: 10.1039/d3ra02812g

rsc.li/rsc-advances

1. Introduction

Transcatheter arterial embolization (TAE) is a minimally invasive interventional procedure widely used in various fields, including intracranial hemorrhagic lesions,[1] and nonmalignant[2] and malignant[3] tumors. The principle for TAE is to block the vessels supplying blood in the target tumor by implementing embolic agents, leading to ischemia and subsequent necrosis of tumor cells.[4–6] For example, uterine artery embolization (UAE) can be applied to treat uterine fibroids, pushing an embolic agent through the uterine artery with a microcatheter to block the blood supply of fibroids, making them shrink and then eventually disappear.[7] Compared with traditional hysterectomy and myomectomy, UAE treatment is advantageous due to its relatively high safety and efficacy, being less invasive, and having fewer complications, and preservation of the uterus.[8] Conventional embolization therapy is usually required to be combined with imaging modalities such as Computed Tomography (CT) to transport the embolic agents to the specific vascular site under image guidance.[9] However, the majority of clinically-used embolic agents, such as poly(vinyl alcohol) (PVA) particles, gelatin sponges, and sodium alginate microspheres, are not characterized by traceability.[10,11] Their visible process was usually achieved when mixed with iodine-based contrast agents.[12] However, due to blood flow, they are easily affected in the vascular system and cannot be continuously tracked.[13,14] The embolic agents may contribute to the non-targeted embolism or reflux into adjacent organs, which is quite dangerous. Therefore, developing new embolic materials to address this issue is significant. Generally, ideal embolic material should have the following characteristics: (1) favorable biocompatibility; (2) easily transportable; (3) certain mechanical intensity; (4) controllability in degradation; (5) traceability.[15] Embolic microspheres are much easier to transport with microcatheters than coils and have excellent mechanical properties that are favorably compared with gel embolic agents. Therefore, researchers have been paying considerable attention to this demandable research area recently.[16]

[a]*Institute of Smart Biomedical Materials, School of Materials Science and Engineering, Zhejiang Sci-Tech University, Hangzhou, 310018, China. E-mail: kongxd@zstu.edu.cn*
[b]*Zhejiang-Mauritius Joint Research Center for Biomaterials and Tissue Engineering, Hangzhou, 310018, China*
[c]*The Department of Medical Imaging, The First Medical College of Zhejiang Chinese Medical University, Hangzhou 310053, China*

† Electronic supplementary information (ESI) available. See DOI: https://doi.org/10.1039/d3ra02812g

Many methods, such as chemical precipitation,[17,18] chemical bonding of the radiopaque moieties,[19] or absorption[20,21] to exploit embolic microspheres with radiopaque properties, have been used to solve the problem that it is difficult to trace the embolic microspheres. However, these fabrication methods are either technically complex or produce non-unform microspheres that are too large for small vessel embolization.[22–24] For example, DC Bead LUMITM and LC Bead LUMITM (70–150 μm and 40–90 μm, respectively), are two radiopaque embolic microspheres with small sizes while non-homogeneous size distribution approved by Food and Drug Administration (FDA).[25,26] In embolization therapy, as the penetration depth of microspheres in the target vessel depends on the depth, controlling the accuracy of microsphere size is of great significance.[27]

Droplet microfluidic techniques are widely used in various fields, especially in life sciences.[28] Compared with continuous flow technology, it has many unique advantages such as fast response, high size controllability, and low cost.[29,30] The monodispersed microdroplets were generated due to the interaction between shear force and surface tension to separate continuous fluid into droplets.[31] Micro-droplet technology can readily provide uniform microspheres, which may be beneficial for controlled embolization, controlled drug release, and enhanced embolization efficiency.[32]

Hyaluronic acid (HA), which largely exists in the extracellular matrix (ECM), is a natural hydrophilic polysaccharide, with amazing biocompatibility and biodegradability.[33] During the past decades, sodium hyaluronate has been widely used in fields such as surgery, tissue engineering, and drug development. 1,4-Butaneglycol diglycidyl ether (BDDE) is a chemical cross-linking agent commonly used to crosslink sodium hyaluronate.[34–36] The mechanical properties of sodium hyaluronate have improved considerably after the cross-linking reaction, and the FDA has deemed HA-BDDE polymer to be used for human implantation.[37,38] However, in the current market, sodium hyaluronate embolization microspheres for commercialized use have not been available. Bismuth-based materials, characterized by notable biocompatibility and incredible X-ray attenuation, have been the subject of interest as a potential contrast agent in CT imaging in recent years.[39,40] Bismuth sulfide (Bi_2S_3) nanorods (NRs) can provide an effective contrast in diagnosing CT imaging disease at an early stage thanks to their existing form of nanoparticles and highly absorbed surface coverage.[41] Compared to conventional contrast agents based on iodine, BSA-Bi_2S_3 NPs synthesized using a simple one-pot method achieved a half-life of nearly 15 h.[42] In addition, it exhibited a clearance rate that can be eliminated from the liver and spleen within 72 h, suggesting the preclinical safety of these NPs.[43] Therefore, preparing embolization microspheres with X-ray impermeability is feasible by physically encapsulating Bi_2S_3 NRs with microspheres.

Based on the above analysis, we have developed an embolic microsphere with uniform size, particle dispersion, X-ray visibility, and favorable biocompatibility in this research. Microspheres mainly comprise sodium hyaluronate and Bi_2S_3 NRs, which are fabricated by simple-step microfluidics. The size distribution, mechanical properties, X-ray visibility, biocompatibility, and *in vitro* simulated embolization of sodium hyaluronate embolization microspheres loaded with Bi_2S_3 NRs have been systematically studied in this paper. It turns out that the fabricated microsphere embolic agent has good X-ray visibility and embolic effect, reflecting a promising applicable potential.

2. Experimental

2.1 Materials

Sodium hyaluronate (MW = 1 000 000–150 000), 1,4-butaneglycol diglycidyl ether (BDDE), normal alkane, isobutanol, and Span 80 were purchased from Aladdin Technology Co., Ltd. Oleylamine, oleic acid, and thioacetamide provided by Heowns Biochemical Technology Co., Ltd. The polymethyl methacrylate (PMMA) microfluidic chip (the width and depth of the channel at the intersection are both 250 μm) was purchased from Beijing LiShi Micro-Nano Technology Co., Ltd. Bismuth neodecanoate was obtained from Shanghai Eon Chemical Technology Co., Ltd. Cell Counting Kit-8 (CCK-8), pancreatic digest, and penicillin/streptomycin was supplied by Beyotime Biotechnology Co., Ltd. Calcein-AM/PI was purchased from Sigma-Aldrich. All the rabbit blood samples were bought from Henan Yuechi Biotechnology Co., Ltd, and its hemolysis assay and blood coagulation test procedures were performed in accordance with the guidelines of Zhejiang Sci-Tech University.

2.2 Characterization

Transmission electron microscopy (TEM) (JEM-2100, Japan), Scanning Electron microscopy (SEM) (ZEISS, USA), and EDS elemental mapping (Carl Zeiss ultra 55, Germany) were employed for the morphological characterization of the various samples. The size distribution of the samples was observed using Malvern Zetasizer Nano ZS instrument (UK) and ImageJ software. The average diameter of the swollen microspheres was divided by the average diameter of the non-swollen microspheres to get the swelling ratio. Fourier transform infrared (FT-IR) spectroscopy (IS 50, Thermo Electron Scientific Corporation, USA) was used to characterize the chemical compositions, with a range from 400 cm^{-1} to 4000 cm^{-1}. The crystal structure of the samples was determined using a powder X-ray diffraction instrument (XRD) (Bruker AXS GMBH, USA) with 2θ ranging from 20.0° to 80.0°. The thermal behavior of the samples was analyzed by Thermogravimetric analysis (TGA), with the temperature gradually increased from 20°C min^{-1} to 30–550 °C (HS-101, Heson, China). The mechanical properties of samples were analyzed by a rheometer at 37 °C (CP5000, LamyETT, China). The dried microsphere samples were swollen in PBS for 24 h, followed by the measurement of the storage modulus (G'), and the loss modulus (G''), at a fixed strain (0.1%) and frequency range of 0.1–100 rads s^{-1} with 10 points per decade, using a microsensing test bench. The X-ray radiopacity of the samples was observed using Xradia 600 Versa Micro-computed tomography (Micro-CT) (ZEISS, USA) and the grayscale value of samples was analyzed by the ImageJ software.

2.3 Synthesis of Bi_2S_3 NRs

Bi_2S_3 NRs were synthesized according to the previous protocols.[44] First of all, 1.45 g of bismuth neodecanoate was added to a mixture of 20 mL of OA and 10 mL of ethanol under stirring conditions. Following this, 4 mL oleylamine solution containing 0.15 g of thioacetamide was promptly introduced to the mixture. The colloidal solution was vigorously stirred for 30 min before being transferred to a 50 mL Teflon-lined autoclave. The was sealed and heated to 150 °C for 10 h, followed gradual cooling to room temperature. The sediments were obtained through centrifugation, washed with ethanol, and placed in an oven at 80 °C for 6 h to dry. Finally, the Bi_2S_3 NRs obtained were lightly ground for further use.

2.4 Fabrication of SH and Bi_2S_3@SH microspheres

A facile one-step microfluidic method was employed to synthesize SH and Bi_2S_3@SH microspheres. To prepare homogeneous gel, 0.4 g sodium hyaluronate powder was solubilized in a 16 mL dilute hydrochloric acid solution (pH = 5), and stirred at 600 rpm for 12 hours. During stirring, BDDE and Bi_2S_3 NPs were added to the solution. The fabricated gel solution was used as the dispersed phase in subsequent experiments. The continuous phase contented liquid paraffin containing 4 wt% Span 80 as a surfactant for fabricating gel microdroplets. The dispersed and continuous phases were maintained at flow rates of 200 μL h^{-1} and 200 μL min^{-1}, respectively, unless otherwise specified. Microdroplets were passed into isobutanol and stirred at 900 rpm for 2 h to break the emulsion and dehydrate. The product was then vacuum dried at 40 °C for 10 h to remove the solvent from the microspheres completely.

2.5 Cytotoxicity

To evaluate the cytotoxicity of the samples, microspheres were sterilized by ultraviolet disinfection for 1 h.[45] Then, 200 mg of each microsphere group was soaked in 15 mL DMEM with 10% fetal bovine serum, and 1% penicillin–streptomycin solution, then placed in an incubator for 24 hours. Subsequently, the microsphere supernatant was subjected to two rounds of filtration by a 0.5 μm strainer. The HUVECs plating density was 6000 cells per well in three 96-well plates and then incubated for 24 h before replacing the original DMEM media with 200 μL microsphere extracts of each group. CCK-8 solution was introduced into individual wells at 24, 48, and 72 h time points. After 1 h incubation, the wavelength of 490 nm was selected to test the absorbance of each well. Live/dead cell assays were performed by co-culturing HUVECs with 20 mg mL^{-1} microspheres in small dishes for 24 and 72 h. The DMEM medium and microspheres were removed at different time points. Next, the Calcein AM and PI were added to stain cells and observed by a confocal laser scanning microscope.

2.6 Hemolysis assay

The hemolysis assay was carried out by using the previously described method.[46] The microspheres of each group (10 mg) were incubated in 1 mL of saline solution for 1 h. Before the hemolysis experiment, citrated whole rabbit blood was diluted 50 times with saline solution and added to centrifuge tubes, covering the bottom of the microspheres. The obtained diluted rabbit blood was mixed with the incubated embolization microsphere solution and incubated at 37 °C for 4 h. Subsequently, the components were centrifuged at 10 000 rpm for 10 min, and the supernatant was collected as the experimental group solution. Negative and positive control groups were represented with saline solution and deionized water, respectively. The absorbance of the supernatant was measured at 545 nm, and the hemolysis rate was calculated through the following equation:

$$\text{Hemolysis (\%)} = (OD_E - OD_N)/OD_P \times 100\%$$

where, OD_E is the absorbance of different samples, OD_N is the absorbance of the negative control, OD_P is the absorbance of the positive control.

2.7 Blood coagulation test

The blood coagulation test of both SH and Bi_2S_3@SH microspheres was evaluated according to the previous protocol, utilizing citrated whole blood from rabbits.[47] Firstly, 10 mg of each microsphere component was incubated in 2 mL of PBS for 1 h at 37 °C. The incubated microspheres were then transferred to a 96-well plate, and 100 μL of sodium citrate anticoagulated rabbit blood was added to each well. Next, 100 μL of $CaCl_2$ solution was added to each well to initiate the coagulation reaction with constant shaking. The clotting reaction was regularly terminated by adding 200 μL of 0.109 M sodium citrate solution and then rinsed thrice with deionized water. Finally, the phenomena in each well were documented by capturing images.

2.8 *In vitro* embolization simulation

To confirm the efficacy and functionality of Bi_2S_3@SH-1 microspheres, *in vitro* simulated embolization tests were performed. A polymethyl methacrylate (PMMA) microfluidic device was used to simulate small-scale blood vessels, with three different vascular diameters set at 800–500, 500–300, and 300 μm, respectively. To observe the embolic effect of Bi_2S_3@SH-1 microspheres in blood vessels of different sizes, the microspheres were mixed with carmine pigment-colored PBS and injected into the microfluidic chip until no further injection was possible.

2.9 Statistical analysis

The results were presented as mean ± standard deviation (SD), and the significance of the difference was analyzed by the *t*-test. The value for $^*P < 0.05$ and $^{**}P < 0.01$ indicated statistical significance and extraordinary statistical significance respectively. The statistical analysis was performed using OriginPro Software.

3. Results and discussion

3.1 Fabrication and characterizations of Bi_2S_3 NRs

Bi_2S_3 NRs have been considered as a potential CT contrast agent due to their high atomic number and X-ray attenuation

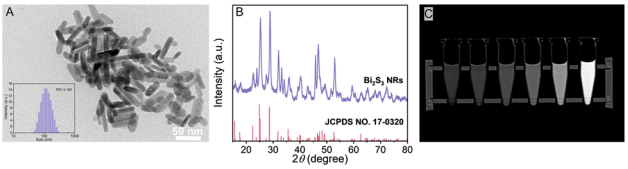

Fig. 1 Characterizations of Bi_2S_3 NRs. (A) TEM image and histogram of the size distribution. (B) XRD spectra. (C) *In vitro* CT images of Bi_2S_3 NRs with different concentrations (2.5, 5, 10, 15, 30, and 60 mg mL^{-1}, from left to right, respectively).

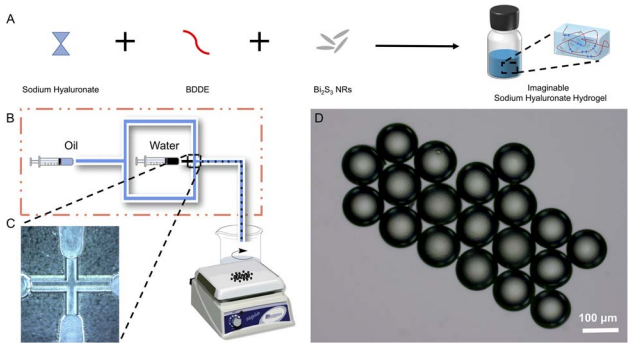

Fig. 2 SH and Bi_2S_3@SH microspheres fabrication schematic: (A) a schematic depicting imaginable (sodium hyaluronate) SH gel fabrication. (B) Schematic depicting microspheres fabrication. (C) Local magnification image of a flow-focused droplet microfluidic chip. (D) Optical micrograph of hydrated SH microspheres.

properties. TEM inspection confirmed that the particles were nano-sized and possessed a rod-shaped structure (Fig. 1A) with a smooth surface and the mean particle size of Bi_2S_3 NRs was 95.4 ± 30.5 nm measured by DLS analysis.[48–50] The results in Fig. 1A indicated that the length of Bi_2S_3 NRs was 50.4 ± 9.2 nm and the width was 11.1 ± 1.9 nm, thereby the aspect ratio of the Bi_2S_3 NRs was close to 4.5. The XRD pattern confirmed the formation of the compound Bi_2S_3 NRs. The diffraction peaks were in accordance with the JCPDS card for Bi_2S_3 NRs (JCPDS card no. 17-0320), as displayed in Fig. 1B. The XRD pattern was well aligned with the orthorhombic structure of Bi_2S_3 NRs. Fig. 1C showed the CT images of Bi_2S_3 NRs synthesized by hydrothermal methods. The brightness of Bi_2S_3 NRs under X-ray increased synchronously with increasing concentration of Bi_2S_3 NRs. The CT images slightly appeared faint due to the insufficient content of Bi_2S_3 NRs (less than 15 mg mL^{-1}). The brightness peak of 60 mg mL^{-1} of Bi_2S_3 NRs reached the maximum. The compositional distribution (EDS) of the Bi_2S_3 NRs was presented in Fig. S1,† which showed the Bi and S elements among the nanocrystals. The fabrication of Bi_2S_3@SH microspheres with X-ray radiopacity was made fundamental by the successful synthesis of Bi_2S_3 NRs.

3.2 Fabrication and characterizations of SH microspheres

The SH microspheres were fabricated by single-step microfluidics, as illustrated in Fig. 2B. The continuous phase (marked with oil) consisted of liquid paraffin containing 4 wt% Span 80, and the dispersed phase (marked with water) consisted of the SH gel. Monodisperse aqueous droplets containing SH gel were prepared due to the interplay between viscosity and capillary forces. Fig. S2† showed that the microdroplets of SH gel were perfectly spherical and well dispersiveness. The microdroplets were demulsified and dehydrated with isobutanol in stirring progress. Compared with traditional methods for the fabrication of microspheres, such as the emulsion method and the spray drying method, microspheres produced by microfluidics have the advantages of uniform size and good dispersibility.

The SH microspheres obtained after vacuum drying had a perfectly spherical shape and quite a smooth surface, no agglomeration between the microspheres occurred, as shown in Fig. 3A–C. The above microspheres had uniform size with an average particle size of 87 μm (Fig. 3D). The SH microspheres vacuum dried were immersed in PBS for swelling, as shown in Fig. 3E. The diameter of the microspheres changed considerably after 24 h. The swelling rate of the microspheres was calculated to be 200.4%. To confirm the successful cross-linking reaction of SH powder with BDDE, it was analyzed by FT-IR, as depicted in Fig. 3F. For the SH microspheres, the peaks at 3363, 2950, and 946 cm^{-1} are ascribed to the stretching vibrations of O–H/N–H bond, C–H band, and C–O–H deformation respectively, demonstrating the successful loading of BDDE into the SH microspheres. Additionally, the C–O stretching vibrations at 910 cm^{-1} that belonged to the BDDE vanished, which indicated the chemical reaction between the –OH group of the SH powder and the C–H band of BDDE. These FT-IR results were consistent with previous research, indicating that the crosslinking reaction between SH and BDDE was operated.[51]

3.3 Characterizations of Bi_2S_3@SH microspheres

For the effective clinical outputs of the SH microspheres, bismuth sulfide (Bi_2S_3), was encapsulated in the fabricated microspheres to achieve imaging-guided embolotherapy. Bi_2S_3 NRs were introduced into the gel solution and physically encapsulated directly during the gel formation process to fabricate the imaginable SH gel (Fig. 2A). The liquid paraffin containing Span 80 (4 wt%) was used as the continuous phase

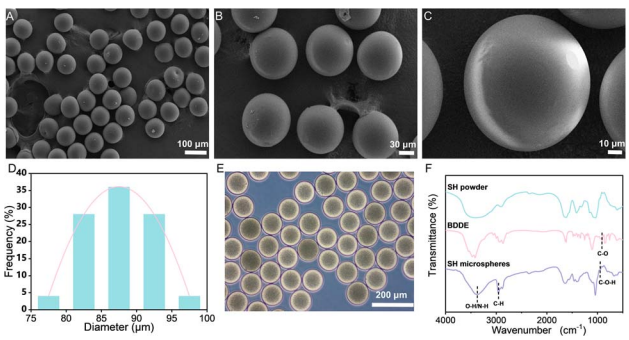

Fig. 3 Characterizations of SH microspheres: (A–C) SEM images of SH microspheres at various magnifications. (D) Histogram of the size distribution of SH microspheres. (E) Optical micrograph of SH microspheres post-swelling in PBS after 24 h. (F) FT-IR spectra of SH powder, BDDE, and SH microspheres.

and the imaginable SH gel was used as the dispersed phase. To fabricate the microdroplets containing imaginable SH gel, the syringes filled with the continuous and dispersed phases are compressed, forcing the liquids through a flow-focusing droplet microfluidic chip. The above microdroplets were dropped into isobutanol for demulsification and drying.

Table S1† shows the composition of different groups of the Bi_2S_3@SH microsphere. The morphologies of the microspheres with and without the loading of Bi_2S_3 NRs were observed by SEM. Fig. 3A and B showed the high magnifications of Fig. 3D and E. The above images showed the surface roughness of the microspheres has increased after loading various contents of Bi_2S_3 NRs on Bi_2S_3@SH microspheres compared to SH microspheres, confirming the successful loading of Bi_2S_3 NRs. However, the Bi_2S_3@SH microspheres were unable to retain the sphere when the content of Bi_2S_3 NRs was high and began to distort or even burst (Fig. 3C, F and S3†). The phenomenon occurred because the excessive addition of Bi_2S_3 NRs during the dehydration process caused the microspheres to become more brittle and thus deformed by centrifugal force when stirring was performed. For loading the Bi_2S_3 NRs with sodium hyaluronate without deformation or rupture, the Bi_2S_3@SH-1 microsphere was selected for the subsequent study. Fig. 3G showed that the SEM image of a single Bi_2S_3@SH-1 microsphere and the schematic of its internal structure was displayed in Fig. 3H. The distribution of Bi_2S_3 NRs on the surface of the single Bi_2S_3@SH-1 microsphere was determined by the EDX mapping images in Fig. 3I–L. Different elements were observed on the surface of the Bi_2S_3@SH-1 microspheres. The elements Bi and S are derived from the Bi_2S_3 NRs, and the elements C and O are derived from the SH matrix. Compared with the previous reports,[16,52] the Bi_2S_3 NRs loaded microspheres were prepared according to the same method, which mixed the NRs and HA physically by stirring over 24 h, increasing the uniform dispersion of Bi_2S_3 NRs within the complex relatively. According to the above results, it could be inferred that the Bi_2S_3@SH-1 microspheres by loading Bi_2S_3 might have excellent X-ray radiopacity (Fig. 4).

The XRD patterns of Bi_2S_3 NRs, SH-0 microspheres, and Bi_2S_3@SH-1 microspheres, as depicted in Fig. 5A. The Bi_2S_3 NRs XRD pattern demonstrated that all diffraction peaks at 15.80°, 17.58°, 22.39°, 28.61°, and 52.61° indexed as typical (020), (120), (220), (211), and (351) planes of Bi_2S_3 crystals, respectively. The above results confirmed that the synthetic NRs were pure Bi_2S_3 with an orthorhombic crystal structure. The bond peak at about 24.4° in the SH-0 microsphere XRD pattern was ascribed to the semicrystalline structure. The characteristic peaks of Bi_2S_3 NRs appeared in the XRD pattern of Bi_2S_3@SH-1 microspheres, which was attributed to introducing Bi_2S_3 NRs into SH-0 microspheres. Furthermore, the characteristic peaks remained distinguishable, demonstrating that Bi_2S_3 NRs exhibited phase stability in the load process, which indicated Bi_2S_3 NRs suitability for embolization applications. Rheological tests are used to analyze the compressibility and flexibility of Bi_2S_3@SH-1 microspheres. The mechanical properties of the microspheres are critical for the embolic effect of the embolized microspheres. The elastic and viscous properties of the material were assessed by the storage and loss moduli at 37 °C, respectively. The storage modulus was used to describe the stiffness of the material. According to previous reports, the storage modulus must be higher than 800 Pa to withstand blood pressure.[53] Fig. 5B exhibited the storage (G') and loss (G'') moduli of microspheres at 37 °C. It is obvious that the G' value was higher than that of G'', and both values were

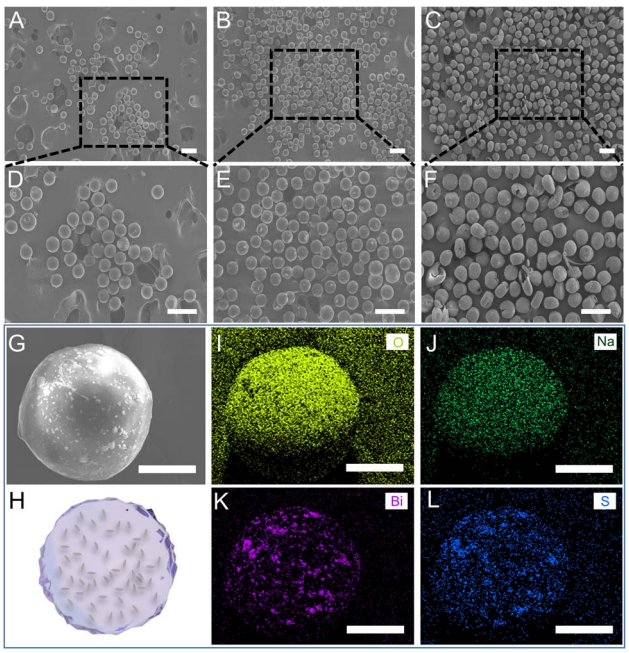

Fig. 4 Characterizations of Bi_2S_3@SH microspheres: (A–C) SEM images of the SH-0, Bi_2S_3@SH-1, and Bi_2S_3@SH-2 microspheres, respectively, scale bar: 200 μm. (D–F) The high magnifications of (A–C), scale bar: 200 μm. (G) The high magnification of a single Bi_2S_3@SH-1 microsphere, scale bar: 30 μm. (H) The schematic of (G) internal structure. (I–L) The EDS-mapping images of (G), scale bar: 30 μm.

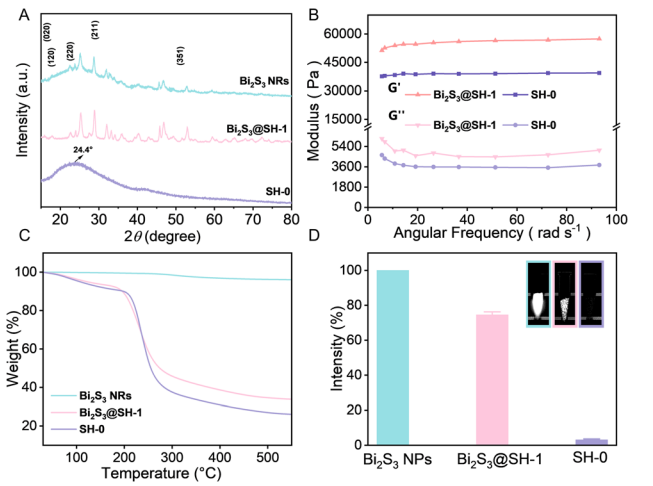

Fig. 5 Characterizations of Bi_2S_3@SH-1 microspheres: (A) XRD spectra. (B) Storage (G') and loss (G'') moduli were recorded for samples. (C) TGA curves of Bi_2S_3 NRs, SH-0, and Bi_2S_3@SH-1 microspheres. (D) *In vitro* CT images and the radiopacity values of the samples ($n = 5$).

unaffected by angular frequencies in the frequency sweep, indicating typical chemically cross-linked gels and the high elasticity of the microspheres. The G' value and G'' value of Bi_2S_3@SH-1 microspheres were both higher than SH-0 microspheres, indicating that the introduction of Bi_2S_3 NRs into the matrix of microspheres could improve the deformation resistance and the flexibility of the microspheres. The phenomenon may be due to the physical mixing of the sodium hyaluronate gel and Bi_2S_3 NRs, which wrapped around the gel chains contribute to improved stiffness and ductility.[54]

To assess the precise content of Bi_2S_3 NRs in Bi_2S_3@SH-1 microspheres, the TGA test was carried out by heating samples from 30 to 550 °C. The Bi_2S_3 NRs showed negligible weight loss, demonstrating excellent thermal stability. The final weight loss percentages of SH-0 and Bi_2S_3@SH-1 microspheres were 74.5% and 64.3%, respectively. The actual content of Bi_2S_3 NRs encapsulated in Bi_2S_3@SH-1 microspheres was calculated to be 10.2%, as illustrated in Fig. 5C. The embolism agents with X-ray visibleness are important to achieve real-time monitoring of intraoperative or postoperative embolotherapy. In this study, Bi_2S_3 NRs have been physically encapsulated in SH matrix for the preparation of radiopacity embolic microspheres. Observation of *in vitro* X-ray radiopacity of SH microspheres, Bi_2S_3@SH-1 microspheres, and pure Bi_2S_3 NRs using Micro-CT. As shown in Fig. 5D, compared to SH microspheres, Bi_2S_3@SH-1 microspheres can be observed under Micro-CT with significant X-ray radiopacity, and the Bi_2S_3 NRs have the strongest signal intensity. Compared with pure Bi_2S_3 NRs, the mean relative percentage of SH-0 microspheres and Bi_2S_3@SH-1 microspheres were 3.56% and 74.42%, respectively. As a result, introducing Bi_2S_3 NRs into the microsphere matrix can effectively enhance its X-ray radiopacity.

3.4 Cytotoxicity test

The ideal embolic agents should have good biocompatibility. Thus, the CCK-8 assay and the Live/Dead cell assay were used to determine the cytotoxicity test of the microspheres in HUVECs. To obtain 20 mg mL^{-1} of microsphere extracts, the culture medium was incubated with the microspheres for 24 h to ensure that the toxic substances in the microspheres had diffused into the medium. The CCK-8 assay was used to determine the cell viability after the extracts of various microspheres were co-cultured with HUVECs for 24, 48, and 72 h. Fig. 6A showed that the cell viability of SH-0, Bi_2S_3@SH-1, and Embosphere microspheres after co-cultured with HUVECs for 24 h was 95.81%, 93.46%, and 95.02%, respectively. After 48 h and 72 h, the cell viability values were all higher than 90%, which followed the *in vivo* toxicity test standard. The above results demonstrated that the extracts of Bi_2S_3@SH-1 microspheres have good biocompatibility *in vitro*. As shown in Fig. 6B, the cytotoxicity test of the microspheres was further determined using the Live/Dead assays, and the morphology of the cells was observed using confocal microscopy after co-culture of the microspheres with the HUVECs for 24 and 72 h, respectively. In contrast to the negative control group, living cells (stained green) exhibited normal growth in distribution and morphology

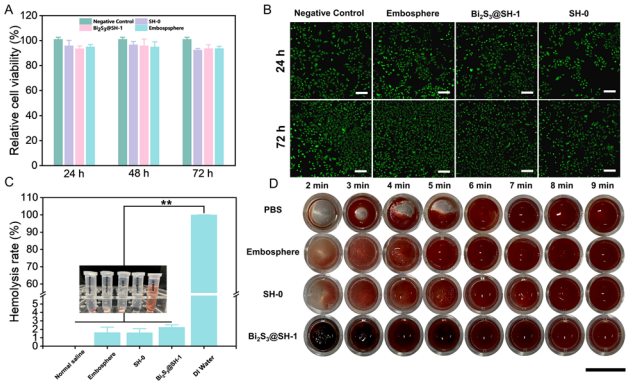

Fig. 6 *In vitro* biocompatibility: (A) the cell viability of HUVECs co-cultured with Bi_2S_3@SH-1 microsphere extracts at 20 mg mL^{-1} for 24 h, 48 h, and 72 h, respectively ($n = 6$). (B) Confocal microscopy images of HUVECs incubated with Bi_2S_3@SH-1 microspheres after 1 and 3 days, scale bar: 200 μm. (C) Hemolysis test of Bi_2S_3@SH-1 microspheres, the insert digital photograph of rabbit carotid blood supernatant and solution after centrifugation of samples, data were shown as mean ± standard deviation, $^{**}p < 0.01$. (D) Blood coagulation test of samples for a different period, scale bar: 1 cm.

on days 1 and 3. The negative control and experiment groups exhibited almost no dead cells (stained red). The Live/Dead assay results demonstrated no adverse effect on the normal growth of cells when the microspheres were co-cultured with HUVECs. Overall, the CCK-8 assay and the Live/Dead assay results demonstrated that the prepared microspheres have good biocompatibility without cytotoxicity.

3.5 Hemocompatibility evaluation

Evaluation of the hemocompatibility of embolic agents is essential due to their direct contact with blood in the body during clinical treatment. Thus, Bi_2S_3@SH-1 microspheres hemolysis assay and blood coagulation test were required. As shown in Fig. 6C that compared with the positive control, the hemolysis ratios of Embosphere, SH-0, and Bi_2S_3@SH-1 were much lower, which were similar to the previous report.[47] The result was also in accordance with the international permissible level of 5% according to the standard of ASTMF/756-08 (2000).[55] The above result suggested that the samples would barely trigger the hemolytic reaction. As shown in Fig. 6D, representative photos of the blood coagulation test were taken at various time intervals. It was seen that there was no discernible difference between SH-0 and Bi_2S_3@SH-1 microspheres and Embosphere, indicating that the clotting times of the Bi_2S_3@SH-1 microspheres were almost the same as that of the commercially available product. Furthermore, the clot sizes of Bi_2S_3@SH-1 microspheres were not less than those of the control groups at each test period. It demonstrated that Bi_2S_3@SH-1 microspheres did not cause slow blood clotting when in direct contact with blood and affected the normal formation of blood clots. Therefore, the above results indicate that the Bi_2S_3@SH-1 microspheres prepared in this study have good hemocompatibility, which grants the microspheres excellent prospects for application in the field of embolization therapy.

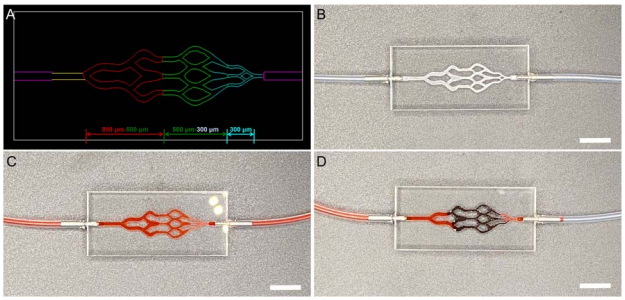

Fig. 7 *In vitro* vascular model embolization: (A) the design image of the PMMA chip. (B) *In vitro* embolization model, scale bar: 1 cm. (C) Before embolization, scale bar: 1 cm. (D) After embolization, scale bar: 1 cm.

3.6 *In vitro* embolization simulation

To investigate the embolic effect and performance of microspheres *in vitro* embolization simulation was carried out. As shown in Fig. 7A and B, PMMA microfluidic chips with different sizes of microfluidic channels were used to simulate small-sized blood vessels. When the above chip was not injected with Bi_2S_3@SH-1 microspheres, PBS (stained with carmine) could quickly flow out of the vascular model (Fig. 7C). PBS (stained with carmine) was mixed physically with Bi_2S_3@SH-1 microspheres and injected into the microfluidic chip until the PBS (stained with carmine) in the flow channel could no longer flow and the injection was stopped, signaling that the embolization process had finished. As shown in Fig. 7D, the microfluidic channels were mainly embolized in the size of 500–300 and 300 μm by Bi_2S_3@SH-1 microspheres, indicating that the Bi_2S_3@SH-1 microspheres fabricated have excellent embolic effect for small-sized blood vessels of 500–300 and 300 μm.

4. Conclusions

In this study, a kind of sodium hyaluronate embolized microspheres were successfully prepared using BDDE as the cross-linker by single-step microfluidics. The fabricated microspheres had uniform size and good dispersibility. Moreover, the rod-shaped Bi_2S_3 CT contrast agents were successfully synthesized by the hydrothermal method. The Bi_2S_3@SH-1 microspheres were prepared by physically encapsulating Bi_2S_3 NRs into the sodium hyaluronate gel. The introduction of Bi_2S_3 NRs improved the mechanical properties of the Bi_2S_3@SH-1 microspheres and endowed them with excellent X-ray radiopacity. Blood compatibility and cytotoxicity test showed that Bi_2S_3@SH-1 microspheres had no blood toxicity and cytotoxicity when used as embolic agents in direct contact with blood and cells, which met international standards. *In vitro*, simulated embolization results indicate that Bi_2S_3@SH-1 microspheres had a good embolization effect. Taken together, compared with traditional embolic microspheres, Bi_2S_3@SH-1 microspheres introduce the imaging function into the embolization microspheres, presenting a simple strategy for the synthesizing of embolization biomedical materials, which further enhances its great potential in precise embolization. Hence, the Bi_2S_3@SH-1 microspheres fabricated by single-step microfluidics in this study have potential application prospects in the field of interventional embolization therapy.

Conflicts of interest

There are no conflicts to declare.

Acknowledgements

This research was financially supported by the National Natural Science Foundation of China (51902289, 51672250), the Natural Science Foundation of Zhejiang Province (LQ22E030018) and the Key Research & Development Program of Zhejiang Province (2021C01180 and 2019C04020).

References

1 J. J. Hu, I. Altun, Z. F. Zhang, H. Albadawi, M. A. Salomao, J. L. Mayer, L. Hemachandra, S. Rehman and R. Oklu, *Adv. Mater.*, 2020, **32**, 2002611.
2 J. J. Hu, H. Albadawi, B. W. Chong, A. R. Deipolyi, R. A. Sheth, A. Khademhosseini and R. Oklu, *Adv. Mater.*, 2019, **31**, 1901071.
3 Y. L. Wang, X. L. He, C. Zhou, Y. W. Bai, T. Q. Li, J. C. Liu, S. G. Ju, C. Y. Wang, G. Y. Xiang and B. Xiong, *Acta Biomater.*, 2022, **154**, 536–548.
4 A. Perez Lopez, C. Martin Sabroso, L. Gomez Lazaro, A. I. Torres Suarez and J. Aparicio Blanco, *Acta Biomater.*, 2022, **149**, 1–15.
5 X. H. Li, M. W. Ullah, B. S. Li and H. R. Chen, *Adv. Healthcare Mater.*, 2023, **41**, 2202787.
6 P. Lv, H. Chen, H. W. Cheng, X. Liu, C. Liu, Y. Zeng, L. Jiang, X. Y. Wang, J. S. Mao and G. Liu, *Adv. Ther.*, 2023, **6**, 2200174.
7 J. Donnez and M. M. Dolmans, *Hum. Reprod. Update*, 2016, **22**, 665–686.
8 I. Manyonda, A. M. Belli, M. A. Lumsden, J. Moss, W. McKinnon, L. J. Middleton, V. Cheed, O. Wu, F. Sirkeci, J. P. Daniels, K. McPherson and F. C. Grp, *N. Engl. J. Med.*, 2020, **383**, 440–451.
9 J. Choi, B. S. Choi, B. Yu, W. G. Li, M. M. Matsumoto, K. R. Harris, R. J. Lewandowski, A. C. Larson, S. K. Mouli and D. H. Kim, *Biomaterials*, 2021, **265**, 120408.
10 J. Zeng, L. Li, H. S. Zhang, J. Y. Li, L. L. Liu, G. F. Zhou, Q. Du, C. S. Zheng and X. L. Yang, *Theranostics*, 2018, **8**, 4591–4600.
11 K. Vogt, L. Aryan, S. Stealey, A. Hall, K. Pereira and S. P. Zustiak, *J. Biomed. Mater. Res., Part A*, 2022, **110**, 131–142.
12 X. J. Han, K. Xu, O. Taratula and K. Farsad, *Nanoscale*, 2019, **11**, 799–819.
13 L. Tian, F. J. Lu, J. Feng and M. P. Melancon, *Acta Pharm. Sin. B*, 2018, **8**, 360–370.
14 J. J. Li, J. H. Wang, J. Y. Li, X. Yang, J. L. Wan, C. S. Zheng, Q. Du, G. F. Zhou and X. L. Yang, *Acta Biomater.*, 2021, **131**, 532–543.
15 C. Y. Wang, J. J. Hu, R. A. Sheth and R. Oklu, *Prog. Biomed. Eng.*, 2020, **2**, 0120023.

16 Z. H. Yi, Z. C. Sun, Y. Shen, D. D. Luo, R. Zhang, S. T. Ma, R. B. Zhao, J. Farheen, M. Z. Iqbal and X. D. Kong, *J. Mater. Chem. B*, 2022, **10**, 4105–4114.
17 C. M. Sommer, U. Stampfl, N. Bellemann, M. Holzschuh, A. Kueller, J. Bluemmel, T. Gehrig, M. Shevchenko, H. G. Kenngott, H. U. Kauczor, P. L. Pereira and B. A. Radeleff, *Invest. Radiol.*, 2013, **48**, 213–222.
18 Q. Wang, D. Zhang, H. B. Xu, X. L. Yang, A. Q. Shen and Y. J. Yang, *Lab Chip*, 2012, **12**, 4781–4786.
19 R. Duran, K. Sharma, M. R. Dreher, K. Ashrafi, S. Mirpour, M. D. Lin, R. E. Schernthaner, T. R. Schlachter, V. Tacher, A. L. Lewis, S. Willis, M. den Hartog, A. Radaelli, A. H. Negussie, B. J. Wood and J. F. H. Geschwind, *Theranostics*, 2016, **6**, 28–39.
20 M. R. Dreher, K. V. Sharma, D. L. Woods, G. Reddy, Y. Q. Tang, W. F. Pritchard, O. A. Chiesa, J. W. Karanian, J. A. Esparza, D. Donahue, E. B. Levy, S. L. Willis, A. L. Lewis and B. J. Wood, *J. Vasc. Intervent. Radiol.*, 2012, **23**, 257–264.
21 V. Tacher, R. Duran, M. D. Lin, J. H. Sohn, K. V. Sharma, Z. J. Wang, J. Chapiro, C. G. Johnson, N. Bhagat, M. R. Dreher, D. Schafer, D. L. Woods, A. L. Lewis, Y. Q. Tang, M. Grass, B. J. Wood and J. F. Geschwind, *Radiology*, 2016, **279**, 741–753.
22 G. Chen, Y. Y. Yang, Q. Xu, M. J. Ling, H. M. Lin, W. Ma, R. Sun, Y. C. Xu, X. Q. Liu, N. Li, Z. Q. Yu and M. Yu, *Nano Lett.*, 2020, **20**, 8141–8150.
23 Y. Y. Yang, Y. J. Yu, H. Chen, X. X. Meng, W. Ma, M. Yu, Z. Y. Li, C. H. Li, H. L. Liu, X. D. Zhang, H. H. Xiao and Z. Q. Yu, *ACS Nano*, 2020, **14**, 13536–13547.
24 W. Ma, Q. L. Chen, W. G. Xu, M. Yu, Y. Y. Yang, B. H. Zou, Y. S. Zhang, J. X. Ding and Z. Q. Yu, *Nano Res.*, 2021, **14**, 846–857.
25 K. Ashrafi, Y. Q. Tang, H. Britton, O. Domenge, D. Blino, A. J. Bushby, K. Shuturminska, M. den Hartog, A. Radaelli, A. H. Negussie, A. S. Mikhail, D. L. Woods, V. Krishnasamy, E. B. Levy, B. J. Wood, S. L. Willis, M. R. Dreher and A. L. Lewis, *J. Controlled Release*, 2017, **250**, 36–47.
26 C. Aliberti, R. Carandina, D. Sarti, E. Pizzirani, G. Ramondo, U. Cillo, S. Guadagni and G. Fiorentini, *Future Oncol.*, 2017, **13**, 2243–2252.
27 C. W. Beh, Y. L. Fu, C. R. Weiss, C. Hu, A. Arepally, H. Q. Mao, T. H. Wang and D. L. Kraitchman, *Lab Chip*, 2020, **20**, 3591–3600.
28 Y. H. Wang, M. Q. Liu, Y. Zhang, H. Liu and L. Han, *Lab Chip*, 2023, **23**, 1080–1096.
29 O. Cybulski, P. Garstecki and B. A. Grzybowski, *Nat. Phys.*, 2019, **15**, 706–713.
30 X. P. Li, D. Li, X. C. Liu and H. L. Chang, *Sens. Actuators, B*, 2016, **229**, 466–475.
31 W. B. Han and X. Y. Chen, *Chem. Eng. Res. Des.*, 2019, **145**, 213–225.
32 Q. Wang, K. Qian, S. S. Liu, Y. J. Yang, B. Liang, C. S. Zheng, X. L. Yang, H. B. Xu and A. Q. Shen, *Biomacromolecules*, 2015, **16**, 1240–1246.
33 J. Y. Zhu, X. D. Tang, Y. Jia, C. T. Ho and Q. R. Huang, *Int. J. Pharm.*, 2020, **578**, 119127.
34 G. Abatangelo, V. Vindigni, G. Avruscio, L. Pandis and P. Brun, *Cells*, 2020, **9**, 1743.
35 H. Kim, H. Jeong, S. Han, S. Beack, B. W. Hwang, M. Shin, S. S. Oh and S. K. Hahn, *Biomaterials*, 2017, **123**, 155–171.
36 G. Y. Lee, J. H. Kim, K. Y. Choi, H. Y. Yoon, K. Kim, I. C. Kwon, K. Choi, B. H. Lee, J. H. Park and I. S. Kim, *Biomaterials*, 2015, **53**, 341–348.
37 S. Lepidi, F. Grego, V. Vindigni, B. Zavan, C. Tonello, G. P. Deriu, G. Abatangelo and R. Cortivo, *Eur. J. Vasc. Endovasc. Surg.*, 2006, **32**, 411–417.
38 K. De Boulle, R. Glogau, T. Kono, M. Nathan, A. Tezel, J. X. Roca-Martinez, S. Paliwal and D. Stroumpoulis, *Dermatol. Surg.*, 2013, **39**, 1758–1766.
39 M. H. Duan, X. Y. Zhu, L. L. Fan, Y. Y. He, C. Yang, R. Guo, S. Chen, X. Y. Sun and J. Liu, *Adv. Mater.*, 2022, **34**, 2205002.
40 Z. Jiang, M. Zhang, P. Li, Y. Wang and Q. Fu, *Theranostics*, 2023, **13**, 483–509.
41 Y. Cai, X. Y. Chen, J. X. Si, X. Z. Mou and X. C. Dong, *Small*, 2021, **17**, 2103072.
42 H. Yu, H. X. Guo, Y. Wang, Y. Y. Wang and L. S. Zhang, *Wiley Interdiscip. Rev.: Nanomed. Nanobiotechnology*, 2022, **14**, e1801.
43 Y. Wang, Y. Y. Wu, Y. J. Liu, J. Shen, L. Lv, L. B. Li, L. C. Yang, J. F. Zeng, Y. Y. Wang, L. S. W. Zhang, Z. Li, M. Y. Gao and Z. F. Chai, *Adv. Funct. Mater.*, 2016, **26**, 5335–5344.
44 J. Liu, X. P. Zheng, Z. J. Gu, C. Y. Chen and Y. L. Zhao, *J. Nanomed. Nanotechnol.*, 2016, **12**, 486–487.
45 J. J. Li, J. H. Wang, J. Y. Li, X. Yang, J. L. Wan, C. S. Zheng, Q. Du, G. F. Zhou and X. L. Yang, *Acta Biomater.*, 2021, **131**, 532–543.
46 X. H. Li, X. F. Ji, K. Chen, M. W. Ullah, X. Yuan, Z. H. Lei, J. M. Cao, J. Xiao and G. Yang, *Biomater. Sci.*, 2020, **8**, 2797–2813.
47 Y. Y. Yang, X. Liu, W. Ma, Q. Xu, G. Chen, Y. F. Wang, H. H. Xiao, N. Li, X. J. Liang, M. Yu and Z. Q. Yu, *Biomaterials*, 2021, **265**, 120456.
48 Z. B. Li, Q. Xu, X. F. Lin, K. Y. Yu, L. Lin, Y. J. Liu and Z. Q. Yu, *Chin. Chem. Lett.*, 2022, **33**, 1875–1879.
49 L. Yu, Z. J. Wang, Z. M. Mo, B. H. Zou, Y. Y. Yang, R. Sun, W. Ma, M. Yu, S. J. Zhang, Z. Q. Yu, T. C. Liu and D. X. Luo, *Acta Pharm. Sin. B*, 2021, **11**, 2004–2015.
50 L. L. Fan, M. H. Duan, Z. C. Xie, K. Q. Pan, X. L. Wang, X. Y. Sun, Q. Wang, W. Rao and J. Liu, *Small*, 2020, **16**, 1903421.
51 S. Bang, D. Das, J. Yu and I. Noh, *Nanomaterials*, 2017, **7**, 328–346.
52 X. Li, X. Ji, K. Chen, M. W. Ullah and G. Yang, *Bioact. Mater.*, 2021, **6**, 2015–2119.
53 A. Fa Timi, F. Zehtabi and S. J. Lerouge, *J. Biomed. Mater. Res., Part B*, 2015, **10**, 1551–1562.
54 Y. J. Seong, G. Lin, B. J. Kim, H. E. Kim, S. Kim and S. H. Jeong, *ACS Omega*, 2019, **4**, 13834–13844.
55 T. Liu, W. Xue, B. Ke, M. Q. Xie and D. Ma, *Biomaterials*, 2014, **35**, 3865–3872.